Optical Injection and Detection of Long-Lived Interlayer Excitons in van der Waals Heterostructures

Alperen Tüğen,[1,*] Anna M. Seiler,[1,*] Arthur Christianen,[1] Kenji Watanabe,[2] Takashi Taniguchi,[3] Martin Kroner,[1] and Ataç İmamoğlu[1]

[1]*Institute for Quantum Electronics, ETH Zurich, CH-8093 Zurich, Switzerland*
[2]*Research Center for Electronic and Optical Materials, National Institute for Materials Science, Tsukuba, Japan*
[3]*Research Center for Materials Nanoarchitectonics, National Institute for Materials Science, Tsukuba, Japan*

(Received 6 June 2025; accepted 3 November 2025; published 10 December 2025)

Interlayer excitons in semiconducting bilayers separated by insulating hexagonal boron nitride (*h*-BN) layers constitute a promising platform for investigation of strongly correlated bosonic phases. Here, we report an optical method for the generation and characterization of long-lived interlayer excitons. We confirm the presence of tightly bound interlayer excitons by measuring 1s and 2s intralayer excitons in each layer concurrently. Using a pump-probe technique, we find interlayer exciton lifetimes up to 8.8 μs, increasing with the thickness of the *h*-BN. With optical access to long-lived interlayer excitons, our approach provides a new route to explore degenerate Bose–Fermi mixtures of excitons and itinerant electrons with high spatial and temporal resolution.

DOI: 10.1103/stgs-2s58

Transition metal dichalcogenide (TMD) heterobilayers have recently emerged as a promising platform for creating long-lived interlayer excitons, bound electron-hole pairs, whose constituents reside in different layers. With their large binding energy and a built-in out-of-plane dipole, they offer a route to investigating many-body phenomena ranging from superfluidity of dipolar excitons [1–4] to Bose–Fermi mixtures exhibiting exotic electron pairing mechanisms [5,6] in van der Waals heterostructures. However, accessing these collective states depends on controlling the lifetime, density, and interactions of interlayer excitons [3,7].

Early demonstrations of long-lived interlayer excitons relied on the electrical injection of charge carriers into separate TMD layers [8–11]. Capacitance spectroscopy and Coulomb-drag measurements provided compelling evidence for interlayer exciton formation. However, these measurements offer no information on time dynamics and spatial distributions. In parallel, optical pumping in aligned $MoSe_2$–WSe_2 bilayers, either in direct contact or separated by one or two hexagonal boron nitride (*h*-BN) layers [12–15], has been explored. Photoluminescence (PL) from such devices has revealed lifetimes up to 1.9 μs [16]. However, achieving longer lifetimes and higher densities requires thicker *h*-BN spacer layers to suppress residual interlayer tunneling and radiative recombination [17]. This, in turn, significantly reduces PL emission, rendering direct optical measurements of the interlayer exciton dynamics untenable.

Here, we demonstrate an optical scheme that overcomes the limitations of both electrical and PL-based injection and detection schemes. While inserting the *h*-BN spacer with up to seven layers to suppress interlayer tunneling, we inject high densities of electrons and holes into separate $MoSe_2$ and WSe_2 layers via nonresonant optical pumping, without requiring layer-selective contacts or complex gating geometries [8,9]. Using time-resolved reflection spectroscopy and the 2s exciton resonance as a spectroscopic probe, we observe interlayer exciton formation and relaxation dynamics in samples with negligible interlayer exciton PL. Under these conditions, we achieve interlayer exciton densities up to $n_{IX} \approx 10^{12}$ cm^{-2} and lifetimes of 8.8 μs. This combination of high density, long lifetime, and optical control opens the door to studying strongly interacting interlayer exciton gases and exploring collective excitonic phenomena.

We investigate three TMD bilayer devices with varying *h*-BN spacers [see Fig. 1(a)]. In the main text, we present data from Devices 1 and 2, both $MoSe_2$–WSe_2 bilayers with *h*-BN spacers of 1- and 3–5-layers, while results from Device 3 (MoS_2–WSe_2, 5–7 layer *h*-BN spacer) are provided in Supplemental Material (SM) [18]. In contrast to previous optical studies, all TMD layers within a device are angle-misaligned, suppressing interlayer hybridization and resulting in negligible interlayer PL [28]. To determine the charge configuration in the individual layers, we perform reflection spectroscopy. The upper panel of Fig. 1(b) shows spectra of the $MoSe_2$ and WSe_2 1s exciton

[*]These authors contributed equally to this work.

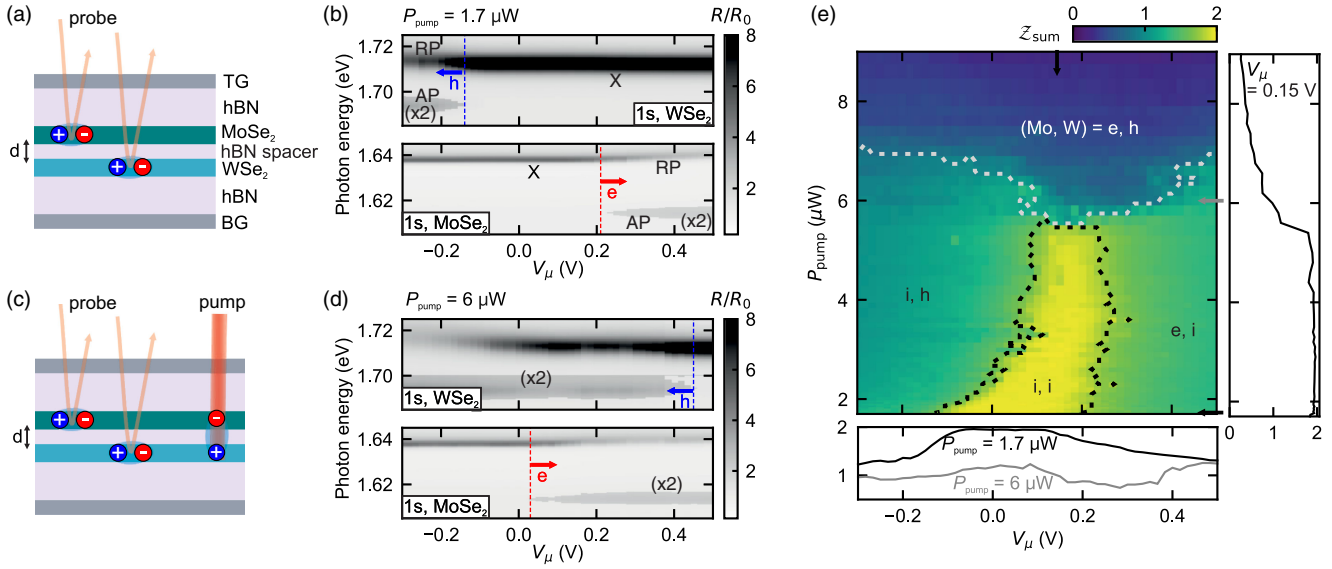

FIG. 1. (a) Schematic of the device structure. (b) Normalized reflection spectra (R/R_0) of the $MoSe_2$ and WSe_2 layers as a function of gate voltage V_μ. Resonances corresponding to the repulsive polaron (RP), attractive polaron (AP), and neutral exciton (X) are indicated. Blue and red dashed lines mark the onset of hole and electron doping, respectively. A weak pump power was present during acquisition ($P_{\text{pump}} = 1.7$ μW); its effect on the spectra is negligible. (c) Schematic under pump conditions. (d) R/R_0 at finite pump power ($P_{\text{pump}} = 6$ μW). (e) The sum of the peak 1s X (RP) reflection contrasts of the $MoSe_2$ and WSe_2 layers, each normalized to its respective reflection contrast in the absence of charges, $\mathcal{Z}_{\text{sum}}$, is shown as a function of V_μ and P_{pump}. Distinct charge configurations are labeled as (i, i), (i, h), (e, i), and (h, e), representing combinations of intrinsic (i), hole (h), and electron (e) doping in the Mo and W layers, respectively. The dotted black contour marks the region where the normalized X (RP) reflection contrast in both layers exceeds 0.7, indicating approximate charge neutrality; note, however, that small but finite doping persists near the boundary of the (i, i) region. The dotted light gray contour outlines the region with opposite doping in the two layers, where the normalized X (RP) reflection contrast in each layer falls below 0.7. Arrows indicate the positions of vertical and horizontal linecuts. Data in panels (b)–(e) were acquired using Device 1.

resonances as a function of the gate voltage V_μ (controls the chemical doping of the layers, see SM [18] for details), measured in Device 1. Upon injection of itinerant charge carriers, the 1s exciton evolves into two distinct resonances [Fig. 1(b)]: the repulsive polaron (RP) and the attractive polaron (AP) [29]. The left (right) side of the blue (red) dashed line in Fig. 1(b) corresponds to hole (electron) injection into the WSe_2 ($MoSe_2$) layer. The voltage range between the dashed lines marks the charge-neutral regime, where neither layer is doped.

Unlike previous experiments that bridged this energy gap using large electric fields and an interlayer bias [8–11], we employ nonresonant optical pumping to inject charge carriers into the TMD bilayer. We illuminate the sample with a continuous-wave laser at 635 nm, above the band gap [Fig. 1(c)] with pump and probe focused onto the same spot. Remarkably, as we show below, this optical doping technique enables simultaneous electron- and hole-doping in opposite layers even for devices with thicker *h*-BN spacers, overcoming the intrinsic band-offset limitations without the need for applying an electrical bias. Figure 1(d) displays the reflection spectra under continuous pumping at laser power $P_{\text{pump}} = 6$ μW. Here, the charge-neutral region vanishes, and we observe simultaneous electron doping in the $MoSe_2$ layer and hole doping in the WSe_2 layer. This is indicated by the reversal in the positions of the red and blue dashed lines [30].

To visualize the overall charge configuration, Fig. 1(e) shows the sum of the peak 1s X (RP) reflection contrast of the $MoSe_2$ and WSe_2 layers normalized to the individual reflection contrast of each layer in the absence of charges ($\mathcal{Z}_{\text{sum}}$) as a function of V_μ and P_{pump} (see SM [18] for details). The yellow region labeled as (i, i) and outlined by a black dotted contour denotes the approximate charge-neutral regime, where both excitons reach maximum contrast. At higher P_{pump}, a dark blue region appears above a light gray dotted contour line, indicating dual-layer doping with opposite charge carriers (e, h). In the surrounding regions, either WSe_2 is hole doped (i, h) or $MoSe_2$ is electron doped (e, i), with the opposite layer remaining charge neutral. Details on the asymmetry between hole and electron doping are provided in SM [18].

Next, we investigate whether the injected electrons and holes form bound interlayer exciton states or remain unbound. Prior theoretical work [31] demonstrated that the modification of the 1s exciton-polaron resonances can be used to differentiate between bound and unbound electron-hole pairs; however, the associated spectral shifts

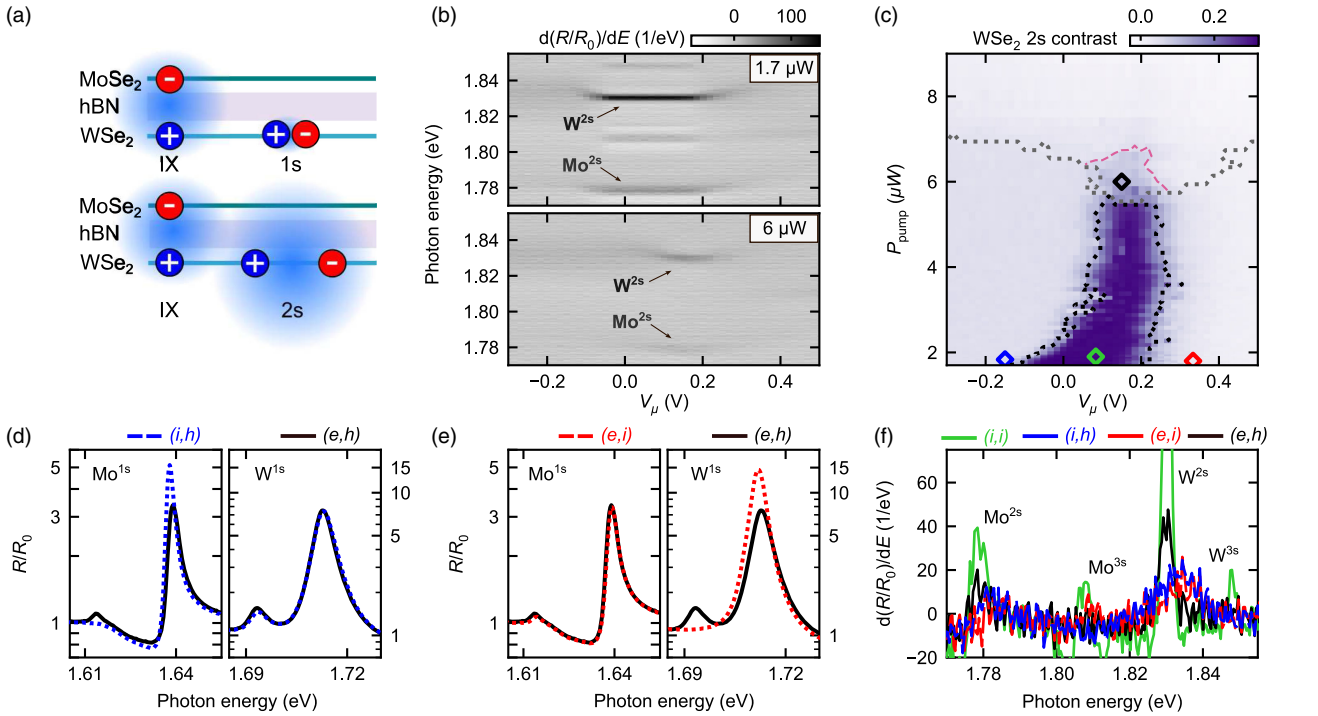

FIG. 2. (a) Schematic of the 1s, 2s intralayer excitons and interlayer exciton (IX). (b) Differential reflection spectra $(\mathrm{d}(R/R_0)/\mathrm{d}E)$ plotted as a function of gate voltage V_μ, in the energy range of the Rydberg excitons. Data are shown for pump powers of $P_{\mathrm{pump}} = 1.7$ μW (upper panel) and $P_{\mathrm{pump}} = 6$ μW (lower panel). $MoSe_2$ and WSe_2 2s Rydberg excitons are labeled (see Fig. S7 [18] for discussion on 3s Rydberg excitons). (c) Color map of WSe_2 2s contrast as a function of V_μ and P_{pump}. The dashed black and gray contour lines delineate different charge configurations, defined as in Fig. 1(e). The dashed pink contour marks the boundary where the WSe_2 2s contrast falls below 0.055 (20%) in the region where the two layers are oppositely doped. (d),(e) Log-scale spectral linecuts at distinct doping configurations [see diamond markers in panel (c)]. The blue and red curves correspond to only hole doping in WSe_2 and only electron doping in $MoSe_2$, respectively, with the opposite layer remaining charge neutral. The black curve shows simultaneous doping of both layers, with individual charge carrier densities matching those in the red and blue cases. (f) Differential reflection spectra $(\mathrm{d}(R/R_0)/\mathrm{d}E)$ plotted across the Rydberg exciton resonances. The green curve, measured at charge neutrality (green diamond), shows the bare Rydberg excitons. The 2s resonance disappears when only one layer is doped (red and blue curves), but remains visible without a significant spectral shift when both layers are doped simultaneously (black curve). Data in panels (b)–(f) were acquired using Device 1.

are rather small and can be masked by exciton line broadening [9]. The origin of this relatively weak dependence is the small Bohr radius of 1s intralayer excitons, rendering them insensitive to the charges in the neighboring TMD layer [see the sketch in the upper panel of Fig. 2(a)]. By contrast, Rydberg exciton states, such as the 2s state, exhibit a significantly larger Bohr radius [lower panel of Fig. 2(a)], making them more sensitive to the surrounding electrostatic environment [32]. As such, the 2s exciton reflection contrast can be expected to respond differently depending on whether the charge carriers are (tightly) bound as interlayer excitons or remain free unbound particles.

Spectrally, we can resolve $MoSe_2$ and WSe_2 2s and 3s excitons in the charge-neutral regime [Fig. 2(b)]. In the case of free carriers residing in the same layer, 2s excitons exhibit a blueshift and loss of oscillator strength even for small carrier densities. When charges are located in the opposite layer, the 2s-resonance still quickly disappears, but part of its oscillator strength is transferred to a new redshifted resonance which arises from the hybridization with the 2p-states [32–35].

Interestingly, we observe that, in the regime where both layers are doped under finite P_{pump}, the $MoSe_2$ and WSe_2 2s exciton features persist with reduced intensity and only a small spectral redshift (see SM [18]). To quantify this behavior across the charge map, we extract the WSe_2 2s contrast, defined as the peak-to-peak amplitude of the dispersive Lorentzian lineshape associated with the WSe_2 2s exciton [Fig. 2(c)]. Figures 2(d)–2(f) show differentiated spectral linecuts taken at different positions in the phase diagram. In the (e, h) regime (black diamond), the 2s exciton contrast remains finite, even though the charge densities match those in the red and blue diamond regions, where the 2s resonance vanishes. Moreover, the 2s resonance energy in the (e, h) region coincides with that at charge neutrality (green diamond). This robustness of the 2s resonance in the presence of dual-layer doping stands in stark contrast to its drastic modification due to free charges in either layer and points to a distinct phase: the formation

of interlayer excitons. Because interlayer excitons are charge neutral and do not generate strong in-plane electric fields, they do not directly hybridize the 2s and 2p-states. Instead, the leading-order interaction between the 2s and interlayer excitons is a weak attractive van der Waals interaction (see SM [18]), leading to a small density-dependent redshift.

We note that the persistence of the 2s was consistently observed at different spots within a device as well as across multiple devices, indicating that spatial inhomogeneities are unlikely to account for the observed feature. Since the measured electron and hole trion binding energies in the two layers agree well with previously studied monolayer devices, we can also rule out strong trapping of the optically introduced charges [36] as an explanation for the robustness of 2s excitons.

We further observe that the 2s exciton contrast diminishes progressively with increasing P_{pump}. This behavior is expected: as the interlayer exciton spacing decreases and approaches the 2s Bohr radius, the 2s state will cease to be bound. The fact that the 3s exciton resonance vanishes at even lower interlayer exciton densities supports our explanation (Fig. S7 [18]). We emphasize that the 2s signal quenches at densities far below the expected interlayer exciton Mott density of $\approx 4 \times 10^{12}$ cm^{-2} [8,31].

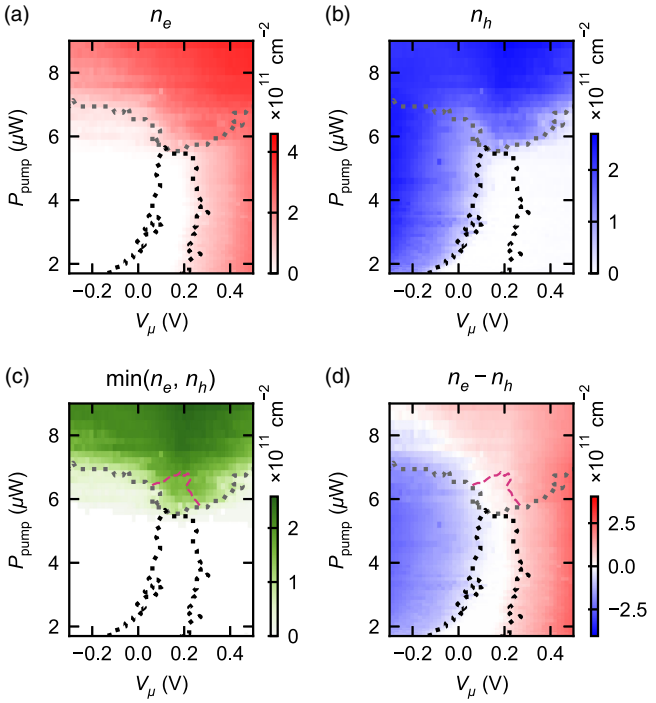

FIG. 3. Charge carrier densities extracted from the optical spectra measured in Device 1 as a function of the gate voltage, V_μ, and pump power, P_{pump}: (a) electron density, n_e, in the $MoSe_2$ layer; (b) hole density, n_h, in the WSe_2 layer; (c) minimum of n_e and n_h [$\min(n_e, n_h)$]; and (d) excess charge $n_e - n_h$. Dotted contour lines denote the same boundaries depicted in Figs. 1(e) and 2(c).

Figures 3(a) and 3(b) show maps of the electron and hole densities, n_e and n_h, as functions of V_μ and P_{pump}, respectively (see SM [18]). From these data we extract the minimum of (n_e, n_h) [$\min(n_e, n_h)$] and the excess charge density $n_e - n_h$, plotted in Figs. 3(c) and 3(d), respectively. In the region where the 2s contrast is visible and the excess charge approaches zero (pink dashed contour), all carriers are paired and thus form interlayer excitons. Thus, the interlayer exciton density is equal to $\min(n_e, n_h)$. Outside the pink contour, interlayer excitons may still be present alongside free carriers, but the 2s spectroscopic signature lacks sufficient contrast to confirm their presence. Here, $\min(n_e, n_h)$ provides an upper bound on the attainable interlayer exciton density. In Device 1, where the $MoSe_2$ and WSe_2 layers are separated by a monolayer of h-BN, the $\min(n_e, n_h)$ reaches up to 3×10^{11} cm^{-2}. By contrast, in Device 2, which features an h-BN spacer thickness of 3–5 layers, $\min(n_e, n_h)$ reaches 1×10^{12} cm^{-2} (Fig. S10 [18]).

Our optical pumping scheme provides access to interlayer exciton dynamics. We probe these dynamics using time-resolved reflection spectroscopy, with synchronized modulation of the pump and probe beams that allows for programmable delays between pulses (see SM [18] for details). In Fig. 4, we present the evolution of $\min(n_e, n_h)$ on a logarithmic scale as a function of pump–probe delay, enabling us to quantify the lifetime of the interlayer exciton state at a representative point in the phase diagram, where $\min(n_e, n_h)$ is finite, the total excess charge is negligible, and the WSe_2 2s exciton is present. The decay of the $\min(n_e, n_h)$ signal with increasing time delay reflects the relaxation of interlayer excitons after the pump laser is turned off. Although the decay is clearly nonexponential, we extract a 1/e lifetime of 1.4 μs for Device 1, which

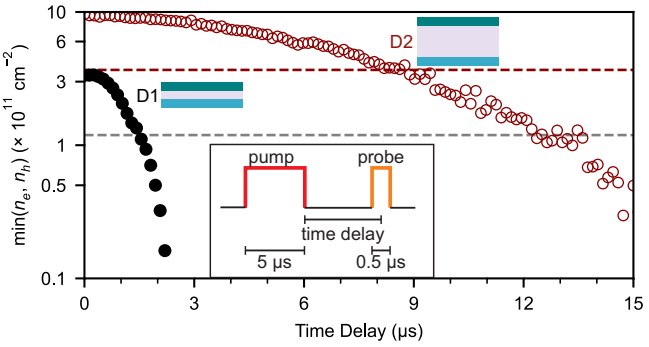

FIG. 4. Time evolution of the minimum of the electron and hole densities, $\min(n_e, n_h)$, as a function of time delay between the pump and probe pulses (see inset). Data points from Device 1 (D1, monolayer h-BN spacer) are shown as black filled circles, while those from Device 2 (D2, 3–5-layer h-BN spacer) are shown as dark red open circles. The dashed lines mark the density at which $\min(n_e, n_h)$ has decayed to $1/e$ of its initial value; the corresponding delay times are 1.4 μs for Device 1 and 8.8 μs for Device 2.

contains a monolayer *h*-BN spacer. By contrast, a significantly longer lifetime of 8.8 μs is observed for Device 2, which has a thicker *h*-BN spacer of 3–5 layers.

This prolonged lifetime is consistent with expectations: increased spacer thickness suppresses interlayer tunneling and reduces the radiative decay rate, thereby extending the interlayer exciton lifetime [16]. Surprisingly, the decay becomes faster at lower carrier densities [37]. We speculate that the shortened lifetime may stem from interlayer excitons becoming more tightly bound as their density is lowered: since the radiative decay rate scales inversely with the square of the Bohr radius, we would expect the lifetime to become shorter. Finally, we emphasize that our measurements cannot rule out a dominant, sample-dependent, nonradiative decay mechanism.

The generation of interlayer excitons within a focused optical spot, combined with the ability to probe their dynamics on picosecond timescales [38], provides a powerful platform for exploring degenerate dipolar excitons with high spatial and temporal resolution. Crucially, it allows for spatially controlled exciton generation without the need for external electric fields, which are typically required in schemes requiring bias voltage for interlayer exciton generation [8,9]. This capability opens the door to creating multiple excitonic reservoirs within a single device, paving the way for Josephson-like experiments [39–41]. In particular, optically inducing high-density exciton populations in two gate-defined traps [42,43] connected by a narrow channel could provide a direct route to optically probing [44] coherent tunneling and phase dynamics between condensate regions.

Acknowledgments—We thank Xiaobo Lu for fabricating Device 1. We thank Ivan Amelio, Haydn S. Adlong, and Igor Khanonkin for inspiring discussions. This work was supported by the Swiss National Science Foundation (SNSF) under Grant No. 200021-204076. A. M. S. and A. C. acknowledge funding from an ETH Postdoctoral Fellowship. K. W. and T. T. acknowledge support from the JSPS KAKENHI (Grants No. 21H05233 and No. 23H02052), the CREST (JPMJCR24A5), JST, and World Premier International Research Center Initiative (WPI), MEXT, Japan.

Data availability—The data that support the findings of this article are openly available [45].

[1] M. Lu, N. Q. Burdick, S. H. Youn, and B. L. Lev, Phys. Rev. Lett. **107**, 190401 (2011).
[2] K. Aikawa, A. Frisch, M. Mark, S. Baier, A. Rietzler, R. Grimm, and F. Ferlaino, Phys. Rev. Lett. **108**, 210401 (2012).
[3] M. Alloing, M. Beian, M. Lewenstein, D. Fuster, Y. González, L. González, R. Combescot, M. Combescot, and F. Dubin, Europhys. Lett. **107**, 10012 (2014).
[4] M. Combescot, R. Combescot, and F. Dubin, Rep. Prog. Phys. **80**, 066501 (2017).
[5] C. Zerba, C. Kuhlenkamp, A. Imamoğlu, and M. Knap, Phys. Rev. Lett. **133**, 056902 (2024).
[6] J. von Milczewski, X. Chen, A. Imamoglu, and R. Schmidt, Phys. Rev. Lett. **133**, 226903 (2024).
[7] A. A. High, J. R. Leonard, A. T. Hammack, M. M. Fogler, L. V. Butov, A. V. Kavokin, K. L. Campman, and A. C. Gossard, Nature (London) **483**, 584 (2012).
[8] L. Ma, P. X. Nguyen, Z. Wang, Y. Zeng, K. Watanabe, T. Taniguchi, A. H. MacDonald, K. F. Mak, and J. Shan, Nature (London) **598**, 585 (2021).
[9] R. Qi, A. Y. Joe, Z. Zhang, Y. Zeng, T. Zheng, Q. Feng, J. Xie, E. Regan, Z. Lu, T. Taniguchi, K. Watanabe, S. Tongay, M. F. Crommie, A. H. MacDonald, and F. Wang, Nat. Commun. **14**, 8264 (2023).
[10] P. X. Nguyen, L. Ma, R. Chaturvedi, K. Watanabe, T. Taniguchi, J. Shan, and K. F. Mak, Science **388**, 274 (2025).
[11] R. Qi, A. Y. Joe, Z. Zhang, J. Xie, Q. Feng, Z. Lu, Z. Wang, T. Taniguchi, K. Watanabe, S. Tongay, and F. Wang, Science **388**, 278 (2025).
[12] P. Rivera, J. R. Schaibley, A. M. Jones, J. S. Ross, S. Wu, G. Aivazian, P. Klement, K. Seyler, G. Clark, N. J. Ghimire *et al.*, Nat. Commun. **6**, 6242 (2015).
[13] L. A. Jauregui, A. Y. Joe, K. Pistunova, D. S. Wild, A. A. High, Y. Zhou, G. Scuri, K. De Greve, A. Sushko, C.-H. Yu *et al.*, Science **366**, 870 (2019).
[14] Y. Shimazaki, I. Schwartz, K. Watanabe, T. Taniguchi, M. Kroner, and A. Imamoğlu, Nature (London) **580**, 472 (2020).
[15] F. Mahdikhanysarvejahany, D. N. Shanks, M. Klein, Q. Wang, M. R. Koehler, D. G. Mandrus, T. Taniguchi, K. Watanabe, O. L. Monti, B. J. LeRoy *et al.*, Nat. Commun. **13**, 5354 (2022).
[16] J. Cutshall, F. Mahdikhany, A. Roche, D. N. Shanks, M. R. Koehler, D. G. Mandrus, T. Taniguchi, K. Watanabe, Q. Zhu, B. J. LeRoy *et al.*, Sci. Adv. **11**, eadr1772 (2025).
[17] D. Snoke, Adv. Condens. Matter Phys. **2011**, 938609 (2011).
[18] See Supplemental Material at http://link.aps.org/supplemental/10.1103/stgs-2s58 for experimental details, additional figures and further discussion, which includes Refs. [19–27].
[19] A. Reinhard, Strong photon-photon interactions in solid state cavity QED, Ph.D. thesis, ETH Zurich, 2013.
[20] J. G. Roch, D. Miserev, G. Froehlicher, N. Leisgang, L. Sponfeldner, K. Watanabe, T. Taniguchi, J. Klinovaja, D. Loss, and R. J. Warburton, Phys. Rev. Lett. **124**, 187602 (2020).
[21] T. Wang, Z. Li, Z. Lu, Y. Li, S. Miao, Z. Lian, Y. Meng, M. Blei, T. Taniguchi, K. Watanabe *et al.*, Phys. Rev. X **10**, 021024 (2020).
[22] E. Liu, J. van Baren, T. Taniguchi, K. Watanabe, Y.-C. Chang, and C. H. Lui, Phys. Rev. B **99**, 205420 (2019).
[23] T. Smoleński, O. Cotlet, A. Popert, P. Back, Y. Shimazaki, P. Knüppel, N. Dietler, T. Taniguchi, K. Watanabe, M. Kroner *et al.*, Phys. Rev. Lett. **123**, 097403 (2019).
[24] J. Kang, S. Tongay, J. Zhou, J. Li, and J. Wu, Appl. Phys. Lett. **102**, 012111 (2013).

[25] P. Rivera, H. Yu, K. L. Seyler, N. P. Wilson, W. Yao, and X. Xu, Nat. Nanotechnol. **13**, 1004 (2018).
[26] Y. Yoon, Z. Zhang, R. Qi, A. Y. Joe, R. Sailus, K. Watanabe, T. Taniguchi, S. Tongay, and F. Wang, Nano Lett. **22**, 10140 (2022).
[27] T. Handa, M. Holbrook, N. Olsen, L. N. Holtzman, L. Huber, H. I. Wang, M. Bonn, K. Barmak, J. C. Hone, A. N. Pasupathy *et al.*, Sci. Adv. **10**, eadj4060 (2024).
[28] Device 1 shows very weak interlayer PL, whereas no interlayer PL is observed in Device 2 or 3; see Fig. S2 in Supplemental Material [18].
[29] M. Sidler, P. Back, O. Cotlet, A. Srivastava, T. Fink, M. Kroner, E. Demler, and A. Imamoglu, Nat. Phys. **13**, 255 (2017).
[30] We emphasize that the two types of doping can be spectrally distinguished in WSe_2 [21]: the presence of a single attractive polaron (AP) resonance in the WSe_2 spectrum unequivocally indicates hole doping since electron doping of WSe_2 leads to two AP features associated with the singlet and triplet trions. By contrast, $MoSe_2$ displays a single AP peak under both electron and hole doping. Additional confirmation comes from Device 3, a MoS_2/WSe_2 heterostructure, where the MoS_2 layer clearly exhibits two AP features under electron doping, consistent with our interpretation of the spectra in Devices 1 and 2 (see Fig. S6 [18]).
[31] I. Amelio, N. D. Drummond, E. Demler, R. Schmidt, and A. Imamoglu, Phys. Rev. B **107**, 155303.
[32] Y. Xu, S. Liu, D. A. Rhodes, K. Watanabe, T. Taniguchi, J. Hone, V. Elser, K. F. Mak, and J. Shan, Nature (London) **587**, 214 (2020).
[33] A. Popert, Y. Shimazaki, M. Kroner, K. Watanabe, T. Taniguchi, A. Imamoğlu, and T. Smoleński, Nano Lett. **22**, 7363 (2022).
[34] J. Kim, H. Dery, and D. Van Tuan, Phys. Rev. B **112**, L041301 (2025).
[35] A. Christianen, A. M. Seiler, A. Tüğen, and A. İmamoğlu (to be published).
[36] N. Kiper, H. S. Adlong, A. Christianen, M. Kroner, K. Watanabe, T. Taniguchi, and A. İmamoğlu, Phys. Rev. X **15**, 011049 (2025).
[37] The parabolic trend in the logarithmic plot in Fig. 4 is clearly visible; similar nonexponential time dependence has also been observed by Cutshall *et al.* [16] in a time-resolved PL measurement.
[38] T. Uto, B. Evrard, K. Watanabe, T. Taniguchi, M. Kroner, and A. İmamoğlu, Phys. Rev. Lett. **132**, 056901 (2024).
[39] B. Khorana, Phys. Rev. **185**, 299 (1969).
[40] K. G. Lagoudakis, B. Pietka, M. Wouters, R. André, and B. Deveaud-Plédran, Phys. Rev. Lett. **105**, 120403 (2010).
[41] M. Abbarchi, A. Amo, V. Sala, D. Solnyshkov, H. Flayac, L. Ferrier, I. Sagnes, E. Galopin, A. Lemaître, G. Malpuech *et al.*, Nat. Phys. **9**, 275 (2013).
[42] R. Rapaport, G. Chen, S. Simon, O. Mitrofanov, L. Pfeiffer, and P. M. Platzman, Phys. Rev. B **72**, 075428 (2005).
[43] A. Gärtner, L. Prechtel, D. Schuh, A. W. Holleitner, and J. P. Kotthaus, Phys. Rev. B **76**, 085304 (2007).
[44] E. C. Regan, D. Wang, C. Jin, M. I. Bakti Utama, B. Gao, X. Wei, S. Zhao, W. Zhao, Z. Zhang, K. Yumigeta *et al.*, Nature (London) **579**, 359 (2020).
[45] A. Tüğen and A. M. Seiler, 2025, 10.3929/ethz-c-000785878.